Advances in Military Technology
Vol. 20, No. 2, 2025, pp. 435-447
ISSN 1802-2308, eISSN 2533-4123
DOI 10.3849/aimt.01986

Mathematical Model of the Current Time of a Five Fragment Nonlinear Frequency Modulated Signal

O. Kostyria[1], A. Hryzo[1*], A. Fedorov[1], H. Khudov[1], Y. Solomonenko[1], and S. Ushakov[2]

[1] *Ivan Kozhedub Kharkiv National Air Force University, Kharkiv, Ukraine*
[2] *National Space Facilities Control and Test Center, Kyiv, Ukraine*

The manuscript was received on 4 April 2025 and was accepted after revision for publication as an original research paper on 13 October 2025.

Abstract:

The paper proposes a mathematical model of a five-fragment nonlinear frequency-modulated signal with a reduced level of the lateral lobes of the autocorrelation function. The decrease in the maximum level of the lateral lobes of the autocorrelation function is due to an increase in the number of signal fragments, a rational choice of their frequency-time characteristics, and compensation of frequency-phase distortions at their junctions. It is shown that this leads to an improvement in the spectral characteristics of the resulting signals. An estimate of the quality of detection of the synthesized signal against the background of reflections from local objects is obtained.

Keywords:

low-altitude target, passive jammer, nonlinear frequency modulation, autocorrelation function, maximum level of side lobes

1 Introduction

The experience of the Air Force units of the Armed Forces of Ukraine shows that the enemy widely uses cruise missiles and Shahed/Geran-type attack drones to strike at the territory of Ukraine. The detection and tracking of such targets by air traffic control radars is difficult due to their small effective scattering surface and flight altitude. For this reason, the maximum detection range of targets of this class by ground surveillance radars is (40–50) km.

It should be noted that ground-based surveillance radars for airspace control traditionally have a maximum detection range of up to 400 km, meaning that the detection of low-altitude targets is significantly affected by the effect of the curvature of the Earth's surface, and targets at low altitudes, starting from a certain range, fall

* *Corresponding author: Research Laboratory, Ivan Kozhedub Kharkiv National Air Force University, Sums'ka st. 77/79, UA-610 23 Kharkiv, Ukraine. Phone: +380 66 210 49 93, E-mail: 166gaa@gmail.com. ORCID 0000-0003-2483-5953.*

into the radio shadow region. For this reason, to ensure the maximum range of detection of targets at small angles, radars of this class have antenna patterns oriented along the line of sight (Fig. 1), i.e., the antenna "lies" on the Earth's surface with its slope at approximately half power level.

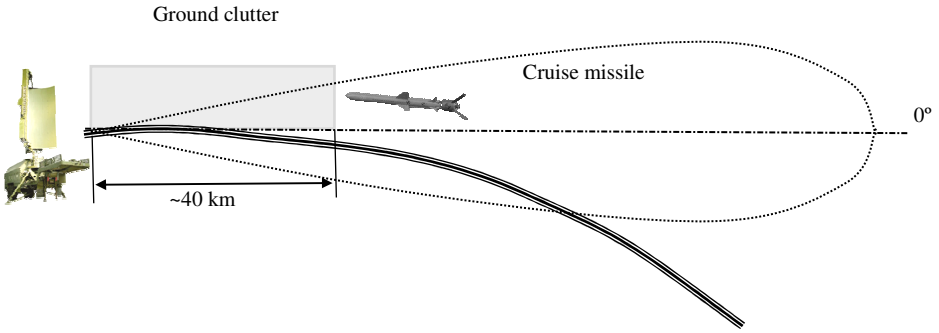

Fig. 1 Orientation of the antenna pattern of a typical airspace control radar

In such conditions, the detection of low-altitude targets in the vast majority of cases occurs in the area of reflections from local objects, the radius of which can be (30-40) km.

When using signals with intra-pulse frequency modulation (complex signals), an important stage of processing is their compression in the time domain [1-4]. This makes it possible to increase the signal-to-noise ratio and provide the required range resolution. The intensity of the compressed signal at the output of a matched filter (MF) varies over time in accordance with its autocorrelation function (ACF), and in addition to the main peak (MP), it has side lobes (SL), which can be quite long in time. For radar signals with linear frequency modulation (LFM), the maximum level of the SL (LSL, MLSL) is approximately −13.5 dB [2].

In the presence of passive interference (PI), SL of the signals reflected from other areas of the range will be superimposed. This leads to a decrease in the degree of non-stationarity of the PI by expanding the areas of influence of reflections from the earth's surface, i.e., to their appearance in areas that were previously free of them. As a result, targets that could previously be observed in the intervals between interference appear to be masked by the SL overlays of compressed signals coming from other range areas. It should be noted that under the influence of long-range powerful reflections, the total background level of the PI can be quite high, which will lead to a deterioration in the quality of detecting echo signals of targets [4].

It is possible to reduce the influence of this effect on the quality indicators of detecting echo signals against the background of nonstationary PI by reducing the MLSL ACF of the sensing signals. A number of papers [5-12] emphasize the expediency of using multifragment nonlinear frequency modulated (NLFM) signals with reduced MLSL ACF, which are described using mathematical models (MM) of several types. In formalizing the description, a mathematical technique is widely used, which consists in using the current or shifted time scale (MM current or shifted time scale). For the current time MM, the description of signal counts is continuous for the entire duration of the radio pulse [5-10]. The difference between the MM of shifted time is that when describing each subsequent signal fragment, the initial time is shifted to zero,

due to which the instantaneous phase and frequency of the signal start from zero [10-12].

Further, as a solution to reduce the negative impact of the SL of ACF of complex signals when detecting them against the background of nonstationary PI, a five-fragment NLFM signal is synthesized. The performance of the new MM NLFM signal consisting of five LFM fragments is confirmed by mathematical modeling. The degree of influence of the SL of ACF on the quality of detection of echo signals in the presence of nonstationary reflections from the earth's surface is estimated. The estimates of the detection quality indicators for different degrees of nonstationarity of the interfering background are obtained, and the results are compared with the case of using a classical LFM signal with equivalent frequency-time parameters.

2 Formulation of Research Task

The aim of this work is to develop a current-time MM of the NLFM signal with a reduced MLSL of the ACF, consisting of five LFM fragments, which provides an improvement in the quality of detecting echo signals under conditions of nonstationary interference background.

3 Presentation of Research Material

3.1 Development of a Mathematical Model of the Current Time for a Five-Fragment NLFM Signal

To develop the current time MM of a five-fragment NLFM signal, we use the model for the case of three LFM fragments with an increasing frequency law as an initial one. The MM of the instantaneous phase of such a signal has the form (1), and it introduces components to compensate for jumps in instantaneous frequency and phase at the joints of the LFM fragments, which ensures minimization of the MLSL of the resulting NLFM signal [6]:

$$\varphi_i(t)\big|_{i=[1,3]} = 2\pi\begin{cases} f_s t + \dfrac{\beta_1 t^2}{2}, & 0 \le t \le T_1 \\ \left(f_s - \delta f_{12}\right)t + \dfrac{\beta_2 t^2}{2} + \delta\varphi_{12}, & T_1 \le t \le \sum\limits_{i=1}^{2} T_i \\ \left(f_s - \delta f_{23}\right)t + \dfrac{\beta_3 t^2}{2} + \delta\varphi_{23}, & \sum\limits_{i=1}^{2} T_i \le t \le \sum\limits_{i=1}^{3} T_i \end{cases} \quad (1)$$

where f_s is the initial (starting) frequency of the NLFM signal; β_i is the frequency modulation rate (FMR) of the corresponding i-th (i = 1, 2, ...) LFM fragment:

$$\beta_i = \frac{\Delta f_i}{T_i}$$

where Δf_i is the frequency deviation of the i-th LFM fragment; T_i is the duration of the i-th NLFM signal fragment; δf_{12} is the instantaneous frequency jump at the junction of the first and second signal fragments [5]:

$$\delta f_{12} = T_1(\beta_2 - \beta_1) \quad (2)$$

δf_{23} – the instantaneous frequency jump at the junction of the second and third fragments [6]:

$$\delta f_{23} = T_1(\beta_3 - \beta_1) + T_2(\beta_3 - \beta_2) \tag{3}$$

$\delta\varphi_{12}$, $\delta\varphi_{23}$ – are the corresponding jumps in the instantaneous phase of the signal at the junctions of the fragments, obtained by integrating (2) and (3):

$$\delta\varphi_{12} = \frac{1}{2}T_1^2(\beta_2 - \beta_1) \tag{4}$$

$$\delta\varphi_{23} = \frac{1}{2}\left[T_1^2(\beta_3 - \beta_1) + T_2^2(\beta_3 - \beta_2)\right] \tag{5}$$

Using the approach and results presented in [6], let us write down the expressions for the instantaneous frequency jumps at the junctions of the third-fourth and fourth-fifth FFT fragments. The analysis of (2) and (3) shows that the addition of each subsequent LFM fragment causes the appearance of a new component of the instantaneous frequency jump. The value of each of the components of the frequency jump is proportional to the product of the difference between the FMR of the current and each of the previous fragments by their respective durations. Thus, for the junctions of the third-fourth and fourth-fifth fragments, we write the following:

$$\delta f_{34} = T_1(\beta_4 - \beta_1) + T_2(\beta_4 - \beta_2) + T_3(\beta_4 - \beta_3) \tag{6}$$

$$\delta f_{45} = T_1(\beta_5 - \beta_1) + T_2(\beta_5 - \beta_2) + T_3(\beta_5 - \beta_3) + T_4(\beta_5 - \beta_4) \tag{7}$$

By analogy to (4), (5), we have:

$$\delta\varphi_{34} = \frac{1}{2}\left[T_1^2(\beta_4 - \beta_1) + T_2^2(\beta_4 - \beta_2) + T_3^2(\beta_4 - \beta_3)\right] \tag{8}$$

$$\delta\varphi_{45} = \frac{1}{2}\left[T_1^2(\beta_5 - \beta_1) + T_2^2(\beta_5 - \beta_2) + T_3^2(\beta_5 - \beta_3) + T_4^2(\beta_5 - \beta_4)\right] \tag{9}$$

Finally, based on (1) and considering (2)-(9), we obtain the MM of the current time of the NLFM signal, which consists of five LFM fragments:

$$\varphi_i(t)\big|_{i=[1,5]} = 2\pi\begin{cases} f_s t + \dfrac{\beta_1 t^2}{2}, & 0 \le t \le T_1 \\ (f_s - \delta f_{12})t + \dfrac{\beta_2 t^2}{2} + \delta\varphi_{12}, & T_1 \le t \le \sum_{i=1}^{2} T_i \\ (f_s - \delta f_{23})t + \dfrac{\beta_3 t^2}{2} + \delta\varphi_{23}, & \sum_{i=1}^{2} T_i \le t \le \sum_{i=1}^{3} T_i \\ (f_s - \delta f_{34})t + \dfrac{\beta_3 t^2}{2} + \delta\varphi_{34}, & \sum_{i=1}^{3} T_i \le t \le \sum_{i=1}^{4} T_i \\ (f_s - \delta f_{45})t + \dfrac{\beta_3 t^2}{2} + \delta\varphi_{45}, & \sum_{i=1}^{4} T_i \le t \le \sum_{i=1}^{5} T_i \end{cases} \tag{10}$$

Let us write MM (10) in a compact form:

$$\varphi_i(t)\big|_{i=[1,5]} = 2\pi\left(f_s - \delta f_{(i-1)i}\right)t + \frac{\beta_i t^2}{2} + \delta\varphi_{(i-1)i}, \qquad \sum_1^{i-1} T_i \le t \le \sum_1^{i} T_i \qquad (11)$$

To verify the validity of the theoretical results presented here, we will conduct a comparative analysis of the oscillograms, spectra, and ACF signals using MM (1) and (11) with respect to the classical LFM signal, provided that their frequency-time parameters are identical.

3.2 Results of Mathematical Modeling

The mathematical modeling was performed using the MATLAB software package. During the simulation, a conventional LFM signal, three- and five-fragment NLFM signals with the same total duration of 140 μs and a frequency deviation of 440 kHz were studied. To provide better visibility of the results and simplify the analysis, the initial frequency of the signals was set to $f_s = 0$.

The modeling has shown that the best values of the MLSL of five-fragment NLFM signals are achieved by observing certain ratios between the duration of the fragments and their frequency deviations. The paper presents the results obtained for the ratio of fragment durations of 1 : 1 : 10 : 1 : 1. For the deviation of the fragment frequency, the values of the FMR are decisive; in the course of modeling, the ratio of the FMR of fragments was used 4 : 2 : 1 : 2 : 4.

The duration of the fragments of the studied NLFM signals was:

- for three fragments $T_1 = T_3 = 20$ μs, $T_2 = 100$ μs,
- in the case of five fragments– $T_1 = T_2 = T_4 = T_5 = 10$ μs, $T_3 = 100$ μs.

The following parameters of ACF signals were evaluated and compared:

- MLSL,
- LSL decay rate,
- the width of the MP of ACF at the level of 0.707 of the maximum value.

Based on the simulation results, Fig. 2 presents the time-domain frequency variation for three- and five-fragment NLFM signals, while Fig. 3 shows the corresponding signal oscillograms, Fig. 4 displays the signal spectra, and Fig. 5 illustrates their autocorrelation functions (ACF).

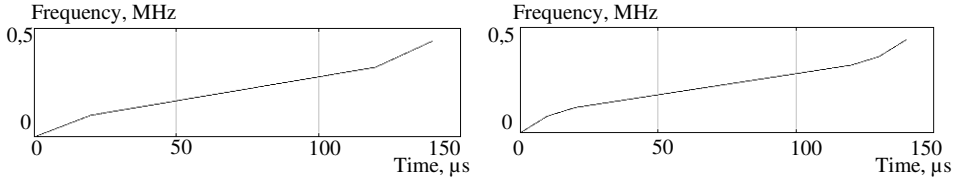

Fig. 2 Frequency variation diagrams of three-fragment (a) and five-fragment, (b) NLFM signals

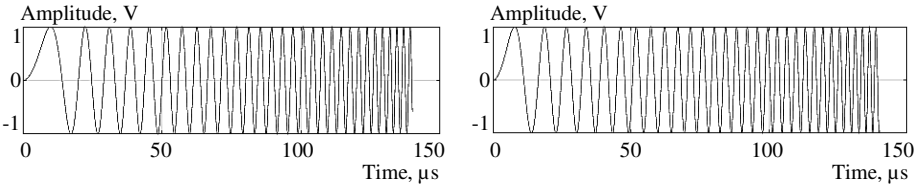

Fig. 3 Oscillograms of three-fragment (a) and five-fragment, (b) NLFM signals

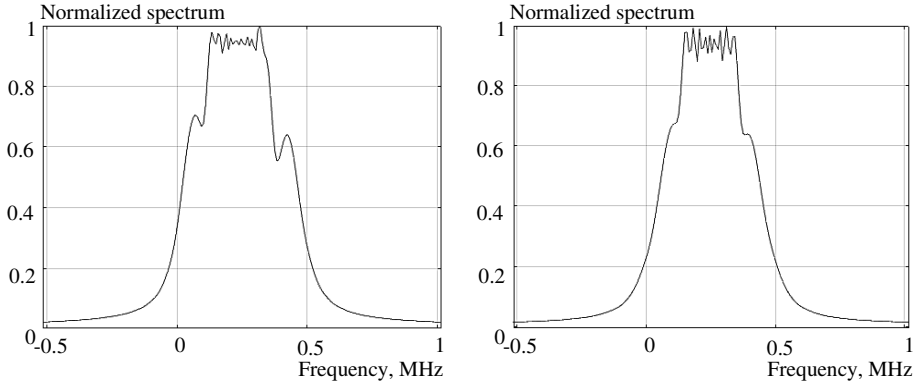

Fig. 4 Spectrum of three-fragment (a) and five-fragment (b) NLFM signals

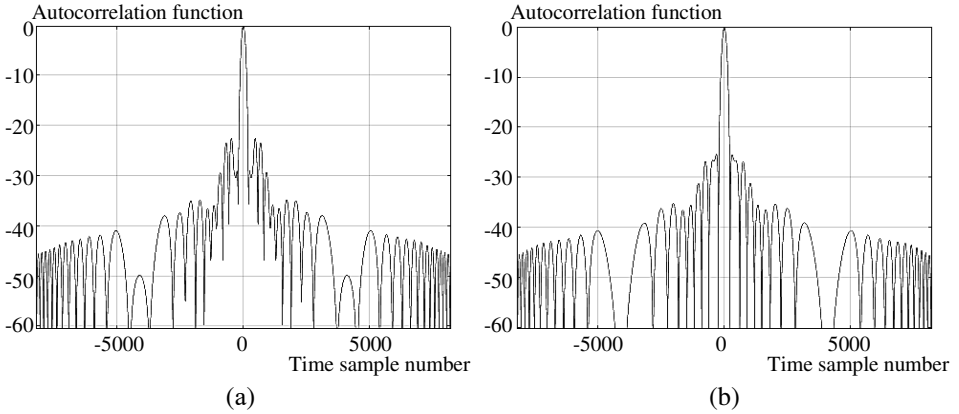

Fig. 5 ACF of three-fragment (a) and five-fragment (b) NLFM signals

The frequency variation graphs of the NLFM signals in Figs 2a and 2b illustrate the number of LFM fragments and the corresponding changes in their slope – i.e., variations in the frequency modulation rate (FMR). Notably, as demonstrated in [5, 6], there are no frequency discontinuities at the junctions between fragments. The graphs are in the same time-frequency range, which indicates the identity of the corresponding signal parameters.

From the analysis of the waveforms of Figs 3a and 3b, it can be seen that there are no jumps in the instantaneous frequency and phase of the signals at the junctions of the fragments for both MM.

The signal spectra of Figs 4a and 4b demonstrate a clear difference: the spectrum of the three-fragment signal has two strongly pronounced modes on the slopes, for the five-fragment signal the modes are less pronounced, the spectrum has a more rounded shape. Both spectra have no discontinuities, dips, or pulsations, which also confirms the absence of jumps in both the instantaneous frequency and phase of the NLFM signals, unlike the results of [5, 6].

The shown ACFs of these signals in Figs 5a and 5b have a similar appearance, which also indicates the equivalence of their time-frequency parameters. In both cases, the nearer SLs form a pedestal near the MP, the main difference being the level of this pedestal relative to the MP maximum; for the five-fragment NLFM signal, this level is clearly lower.

Tab. 1 shows the numerical values of the ACF parameters of the LFM and NLFM signals and the results of their comparison. The parentheses show the change in the value of the selected parameter ("+" – increase, "–" – decrease) relative to the LFM signal.

Tab. 1 Results of comparing the parameters of ACF LFM and NLFM signals

Parameter name	LFM	NLFM 3 fragments	NLFM 5 fragments
Width of ML of the ACF, [μs]	2.0	2.49 (+25 %)	2.74 (+36 %)
MLSL, [dB]	−13.47	−22.62 (−68 %)	−25.45 (−89 %)
The rate of decay of the SL, [dB/dec]	20.13	18.4 (−9 %)	13.65 (−32 %)

Fig. 6 presents a graphical comparison of the signals based on the data from Tab. 1. The signals are compared by the width of the main lobe of the ACF and the value of the MLSL – these parameters are the most critical in the vast majority of practical applications.

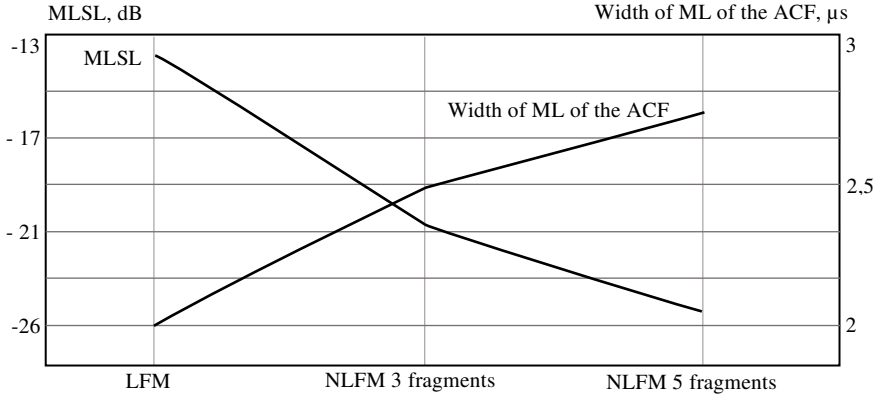

Fig. 6 Comparison of parameters LFM, three-fragment and five-fragment NLFM signals

The analysis of the results indicates a lower value of the MLSL of both the three-fragment and the proposed five-fragment NLFM signals compared to the known LFMs. The MLSL reduction of the five-fragment NLFM signal compared to the three-fragment signal is 12.5 %, and the relative expansion of MP of the ACF in this case is 10 %.

A lower value of the LSL decay rate for the synthesized signal is associated with a significant decrease in the MLSL dB compared to the LFM signal at a time when the level of remote SLs changes little.

It should be noted that in modern radar systems, the generation and processing of radar signals are performed by software tools. Under such conditions, when maintaining equivalent time-frequency parameters, the introduction of various types of NLFM signals requires only changes to the software code according to the desired MM, without any modifications to the hardware.

3.3 Estimation of Degree of Influence of MLSL and Shape of ACF on Quality of Echo Detection Under Influence of Reflections from Earth's Surface

Real reflections from local objects can occupy up to 50 % of the detection area and, as a rule, have an average power of 30 dB to 40 dB and a non-stationary distribution over space elements. For example, Fig. 7 shows photographs of the screens of a centimeter-wavelength radar indicator obtained in a field experiment. By selecting the display threshold, it is possible to estimate the spatial distribution of PI that exceeds it.

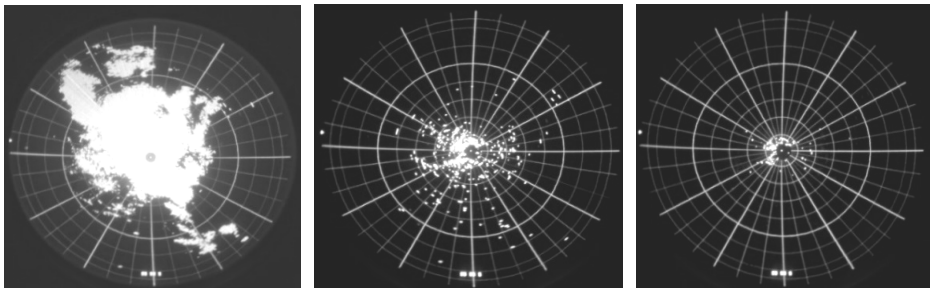

threshold 6 dB | threshold of 36 dB | threshold 72 dB

Fig. 7 Photos of the radar angle indicator, the indicator scale is 75 km

Determination of the level of the PI acting in the path is provided by the PI detection channel in the radar. The threshold for detecting the PI can be set relative to the intrinsic noise level of the receiving path from 0 dB to 42 dB with a 6 dB resolution. This allows you to estimate the power of reflections from local objects and their location. Additionally, up to a range of 6.7 km, attenuation from 10 dB to 30 dB in 5 dB increments can be introduced using the Time-Varied Gain (TVG) device. Thus, a maximum attenuation of 72 dB can be set at a range of up to 6.7 km.

The analysis of Fig. 7 shows that, despite the flat nature of the position, the zone of reflections from the earth's surface can extend up to (40-60) km, and the interference levels in local places at short range exceed 70 dB. A closer look reveals a significantly pronounced discrete nature of the reflections. The interference levels in adjacent elements of the distinction can differ by (30-60) dB. The vast majority of interference has a power of (20-40) dB.

We will assume that the random samples of processes in each of the detection elements have a Rayleigh distribution of amplitude and a uniform distribution of the

initial phase, under which conditions the optimal detection algorithm is reduced to comparing the modular value of the weighted sum at the MF output with its threshold.

As indicators of detection quality, we use the conditional probability of correct detection D and false alarm F. Assuming that for each k^{th} element of the space its modular value of the weighting sum is calculated, for a signal with a random amplitude distributed according to the Rayleigh law and a uniformly distributed initial phase, we will have a partial value of the conditional probability of correct detection (F = const) [1, 3, 4]:

$$D_i = F^{\left(1+\frac{q_k^2}{2}\right)^{-1}} \tag{12}$$

where q_k^2 is the detection parameter that determines the signal/interference + noise ratio in the k^{th} element of space. For certain conditions, the detection parameter is equal to [1, 4]:

$$q_k^2 = q(\sigma_{\text{PI},k}^2)^2 = 2\frac{\sigma_S^2}{\sigma_N^2 + \sigma_{\text{PI},k}^2} \tag{13}$$

where $\sigma_{\text{PI},k}^2$ is the power of the passive interference samples in the k^{th} space element; σ_S^2 is the power of the useful signal samples; σ_N^2 is the power of the intrinsic noise samples ($\sigma_N^2 = 1$).

For further analysis, we will obtain the average value of the probability of correct detection over the elements of the space. Such a problem belongs to the class of problems with parametric a priori uncertainty [13]. General approach to solving such problems is to use the full probability formula to move from the conditional probability density D_k (12) to the unconditional probability density D by averaging over the value of the unknown parameter (13), i.e., in fact, over the distribution of the passive interference power value $\sigma_{\text{PI},k}^2$.

To move from the partial to the average value of the probability of correct detection D, it is necessary to set a distribution law that describes the statistical characteristics of the parameter $\sigma_{\text{PI},k}^2$. To do this, it is convenient to use the generalized distribution of PI power introduced in [14] (for simplicity, $\sigma_{\text{PI},k}^2 = \sigma^2$):

$$W\left(\sigma^2, m, \Delta\right) = \frac{\left(\sigma^2\right)^{\Delta^{-2}-1}}{\left(m\Delta^2\right)^{\Delta^{-2}} G\left(\Delta^{-2}\right)} \exp\left(-\frac{\sigma^2}{m\Delta^2}\right) \tag{14}$$

where $G(z)$ is the gamma function; m is the average value of the PI power relative to the intrinsic noise level, [dB]; Δ is the average power fluctuation range relative to m, [dB].

The generalized PI power distribution (14) belongs to the Family of Generalized Gamma Distributions and generalizes a number of unimodal laws [15-18]. The use of (14) makes it possible to set different levels of nonstationarity of the interfering background by changing the magnitude of power fluctuations Δ while maintaining its average value m.

The final expression for calculating the average value of the probability of correct detection is as follows:

$$D = \int_0^{\infty} F^{\left(1+\frac{\sigma^2}{\sigma_N^2+\sigma^2}\right)^{-1}} W\left(\sigma^2, m, \Delta\right) \mathrm{d}\sigma^2 \tag{15}$$

We will evaluate the effect of the SL ACF of the proposed MM signal (11) on the detection quality indicators against the background of non-stationary PI by mathematical modeling. The results will be compared with those obtained for a conventional LFM signal with equivalent frequency and time parameters.

For the simulation, initial realizations of the intensity distribution of the unsteady PI by range elements with known parameters m = 30 dB and Δ = 3 dB, Δ = 5 dB, Δ = 10 dB were generated, which corresponds to most practical situations. Next, for the selected signal, the MF responses were summed sequentially by range elements. New values of the parameters m and Δ were determined for the output sequences obtained in this way. Finally, for the selected false alarm value, the conditional probability of correct detection was calculated using formula (15).

The results of the calculations are shown in Fig. 8. The detection curves are plotted for the conditional false alarm probability $F = 10^{-6}$. For comparison, two extreme cases are presented - no interference and the presence of a stationary interference with an intensity of 30 dB. Curves 1 and 2 correspond to the level of non-stationarity of the PI Δ = 10 dB, curves 3, 4 and 5, 6 to the levels Δ = 5 dB and Δ = 3 dB, respectively. The dashed curve corresponds to the proposed model of the NLFM signal (curves 1, 3, 5), and the solid curve corresponds to the LFM signal (curves 2, 4, 6).

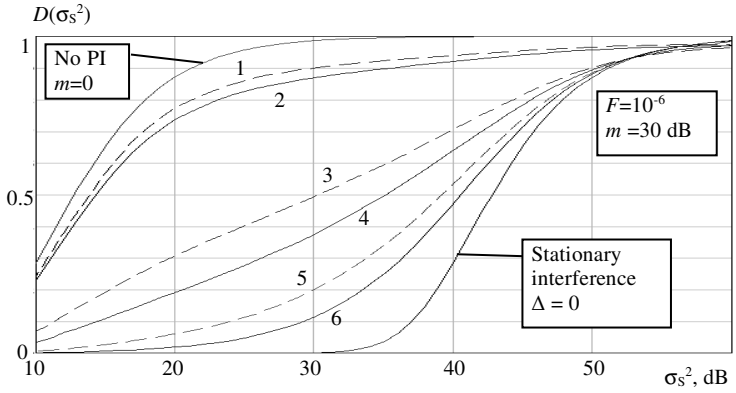

Fig. 8 Detection curves for different signal models

The analysis of the curves shows that the higher the level of nonstationarity of the interfering background (Δ = 10 dB, curves 1 and 2), the greater the potential gain in the signal-to-interference-plus-noise ratio. Physically, this is explained by the fact that almost all the PIs are localized in individual elements of the detection, and the target can be observed in the interference gaps. The process at the MF output exhibits strong, intermittent bursts of energy interspersed with extended periods of low power. Under these conditions, the shape of the ACF and the value of its MLSL have minimal impact. In fact, it is a matter of detecting echo signals of targets against the background of their own noise. The difference in the course of curves 1 and 2 is no more than 1 dB, and they are close to the case of no interference.

As the level of nonstationarity of the AS decreases (Δ = 5 dB, curves 3 and 4), the shape of the ACF and the value of its MLSL begin to have a more significant impact. Physically, this is explained by the fact that the areas occupied by the RI become more frequent, the RI reflections from different range areas overlap, the RI level increases, and the areas that were previously free of it are filled (the "stretching" effect). The model with a lower MRBP value is expected to give a better result, with an energy gain of 5 dB compared to the LFM signal.

As the nature of the interfering background approaches the stationary one (Δ = 3 dB, curves 3, 4), the difference in the curves decreases and amounts to (1.5-2.0) dB. This is due to a decrease in the number of areas with a low level of PI, the curves for both signal models are approaching the case of a stationary interference with the corresponding power level.

Note that for all cases, the gain is more noticeable with reduced requirements for signal detection quality D = (0.3–0.5) and can be (6–7) dB.

4 Conclusions

In this paper, we first developed a current-time MM of the NLFM signal, which consists of five LFM fragments. An increase in the number of fragments allows for a smoother change in the FMR of the signal, which provides better rounding of its spectrum. Due to this, the MLSL of the five-fragment NLFM signal is reduced by 11.98 dB compared to the LFM and is −25.45 dB for the specified frequency-time parameters

For the first time, we derived a relation for finding the components that compensate for instantaneous frequency and phase jumps at the junctions of the third-fourth and fourth-fifth LFM fragments.

Compared to the classical LFM signal, the proposed five-fragment NLFM signal provides an 89 % reduction in the MLSL, which is its undoubted advantage, but the price for this is a 36 % deterioration in range resolution. Therefore, when resolution is critical for practical applications, the use of such a signal necessitates a proportional increase in the product of frequency deviation and signal duration.

The effectiveness of the synthesized signal in detecting airborne targets against the background of reflections from local objects is evaluated. Reducing the MLSL provides an energy gain in target detection from 1.5 dB to 5 dB, depending on the level of nonstationarity of the interfering background.

The practical application of the proposed five-fragment NLFM signal will improve the tactical and technical characteristics of radar means for detecting small-sized objects by increasing the probability of correct target detection against the background of non-stationary PI.

A future study is planned to compare the three-fragment and five-fragment NLFM signals with other well-known NLFM waveforms under equivalent time-frequency conditions.

Acknowledgement

We thank the management of Ivan Kozhedub Kharkiv National Air Force University for the opportunity to conduct scientific research.

References

[1] SKOLNIK, M.I. *Introduction to Radar Systems*. New York: McGraw Hill, 1980. ISBN 0-07-288138-0.

[2] COOK, C.E. and M. BERNFELD. *Radar Signals: An Introduction to Theory and Application*. Boston: Artech House, 1993. ISBN 0-89006-733-3.

[3] LEVANON, N. and E. MOZESON. *Radar Signals*. New York: Wiley, 2004. ISBN 0-471-47378-2.

[4] MELVIN, W.L. and J.A. SCHEER. *Principles of Modern Radar: Advanced Techniques*. Southampton: SciTech Publishing, 2012. ISBN 1-891121-53-7.

[5] KOSTYRIA, O., A. HRYZO, O. DODUKH and O. NARIEZHNII. Mathematical Model of a Two-Fragment Signal with a Non-Linear Frequency Modulation in the Current Period of Time. *Visnyk NTUU KPI Seriia – Radiotekhnika Radioaparatobuduvannia*, 2023, **92**, pp. 60-67. DOI 10.20535/RADAP.2023.92.60-67.

[6] KOSTYRIA, O., A. HRYZO, O. DODUKH, O. NAREZHNYI and A. FEDOROV. Mathematical Model of the Current Time for Three-Fragment Radar Signal with Non-Linear Frequency Modulation. *Radio Electronics, Computer Science, Control*, 2023, **3**(66), pp. 17-26. DOI 10.15588/1607-3274-2023-3-2.

[7] KOSTYRIA, O., A. HRYZO, O. DODUKH, B. LISOHORSKYI and A. LUKIANCHYKOV. Method of Minimization Sidelobes Level Autocorrelation Functions of Signals with Non-linear Frequency Modulation. *Radio Electronics, Computer Science, Control*, 2023, **4**(67), pp. 39-48. DOI 10.15588/1607-3274-2023-4-4.

[8] KOSTYRIA, O., A. HRYZO, Y. SOLOMONENKO, O. DODUKH and Y. BIERNIK. Mathematical Model of Shifted Time of Combined Signal as Part of Fragments with Linear and Quadratic Frequency Modulation. *Visnyk NTUU KPI Seriia – Radiotekhnika Radioaparatobuduvannia*, 2024, **97**, pp. 5-11. DOI 10.20535/RADAP.2024.97.5-11.

[9] KOSTYRIA, O., A. HRYZO, H. KHUDOV, O. DODUKH and Y. SOLOMONENKO. Mathematical Model of Current Time of Signal from Serial Combination Linear-Frequency and Quadratically Modulated Fragments. *Radio Electronics, Computer Science, Control*, 2024, **2**(69), pp. 24-33. DOI 10.15588/1607-3274-2024-2-2.

[10] KOSTYRIA, O., A. HRYZO, H. KHUDOV, O. DODUKH and B. LISOHORSKYI. Two-Fragment Non-Linear-Frequency Modulated Signals with Roots of Kuadratic and Linear Laws Frequency Changes. *Radio Electronics, Computer Science, Control*, 2024, **1**(68), pp. 17-27. DOI 10.15588/1607-3274-2024-1-2.

[11] KOSTYRIA, O., A. HRYZO, O. DODUKH and O. NARIEZHNII. Improvement of Mathematical Models with Time-Shift of Two- and Tri-Fragment Signals with Non-Linear Frequency Modulation. *Visnyk NTUU KPI Seriia – Radiotekhnika Radioaparatobuduvannia*, 2023, **93**, pp. 22-30. DOI 10.20535/RADAP.2023.93.22-30.

[12] KOSTYRIA, O., A. HRYZO, I. KHIZHNYAK, A. FEDOROV and A. LUKIANCHYKOV. Implementation of the Method of Minimizing the Side Lobe Level of Autocorrelation Functions of Signals with Nonlinear Frequency

Modulation. *Visnyk NTUU KPI Seriia – Radiotekhnika Radioaparatobuduvannia*, 2024, **95**, pp. 22-30. DOI 10.20535/RADAP.2023.93.22-30.

[13] FELLER, W. *An Introduction to Probability Theory and its Applications*. *Vol. 2*. 2nd ed. New York: Wiley, 1991. ISBN 0-471-25709-5.

[14] HRYZO, A., O. KOSTYRIA, A. FEDOROV, A. LUKIANCHYKOV and Ye. Biernik. Assessment of the Quality of Detection of a Radar Signal with Nonlinear Frequency Modulation in the Presence of a Non-stationary Interfering Background. *Radio Electronics, Computer Science, Control*, 2025, **1**(72), pp. 18-26. DOI 10.15588/1607-3274-2025-1-2.

[15] STACY, E.W. A Generalization of the Gamma Distribution. *Annals of Mathematical Statistics*, 1962, **33**(3), pp. 1187-1192. DOI 10.1214/aoms/ 1177704481.

[16] ALZAATREH, A., C. LEE and F. FAMOYE. Family of Generalized Gamma Distributions: Properties and Applications. *Hacettepe Journal of Mathematics and Statistics*, 2016, **45**(3), pp. 869-886. DOI 10.15672/HJMS.20156610980.

[17] KICHE, J., O. NGESA and G. ORWA. On Generalized Gamma Distribution and its Application to Survival Data. *International Journal of Statistics and Probability*, 2019, **8**(5), pp. 85-102. DOI 10.5539/ijsp.v8n5p85.

[18] SPORTOUCHE, H., J.-M. NICOLAS and F. TUPIN. Mimic Capacity of Fisher and Generalized Gamma Distributions for High-Resolution SAR Image Statistical Modeling. *IEEE Journal of Selected Topics in Applied Earth Observations and Remote Sensing*, 2017, **10**(12), pp. 5695-5711. DOI 10.1109/JSTARS. 2017.2747118.